ORIGINAL ARTICLE

Dynamics of Ionic Shifts in Cortical Spreading Depression

Rune Enger[1,2,3], Wannan Tang[2,3,4,†], Gry Fluge Vindedal[2,3,†], Vidar Jensen[2,3],
P. Johannes Helm[3], Rolf Sprengel[4], Loren L. Looger[5], and
Erlend A. Nagelhus[1,2,3,4]

[1]Department of Neurology, Oslo University Hospital, 0027 Oslo, Norway, [2]Centre for Molecular Medicine Norway,
Nordic EMBL Partnership, University of Oslo, 0318 Oslo, Norway, [3]Department of Molecular Medicine, Letten
Centre and GliaLab, Institute of Basic Medical Sciences, University of Oslo, 0317 Oslo, Norway, [4]Department of
Molecular Neurobiology, Max Planck Institute for Medical Research, D69120 Heidelberg, Germany, and [5]Janelia
Farm Research Campus, Howard Hughes Medical Institute, Ashburn, VA 20147, USA

Address correspondence to Erlend A. Nagelhus, Letten Centre and GliaLab, Department of Molecular Medicine, Institute of Basic Medical Sciences, University
of Oslo, 0317 Oslo, Norway. Email: e.a.nagelhus@medisin.uio.no

[†]Wannan Tang and Gry Fluge Vindedal contributed equally to this work.

Abstract

Cortical spreading depression is a slowly propagating wave of near-complete depolarization of brain cells followed by temporary suppression of neuronal activity. Accumulating evidence indicates that cortical spreading depression underlies the migraine aura and that similar waves promote tissue damage in stroke, trauma, and hemorrhage. Cortical spreading depression is characterized by neuronal swelling, profound elevation of extracellular potassium and glutamate, multiphasic blood flow changes, and drop in tissue oxygen tension. The slow speed of the cortical spreading depression wave implies that it is mediated by diffusion of a chemical substance, yet the identity of this substance and the pathway it follows are unknown. Intercellular spread between gap junction-coupled neurons or glial cells and interstitial diffusion of K^+ or glutamate have been proposed. Here we use extracellular direct current potential recordings, K^+-sensitive microelectrodes, and 2-photon imaging with ultrasensitive Ca^{2+} and glutamate fluorescent probes to elucidate the spatiotemporal dynamics of ionic shifts associated with the propagation of cortical spreading depression in the visual cortex of adult living mice. Our data argue against intercellular spread of Ca^{2+} carrying the cortical spreading depression wavefront and are in favor of interstitial K^+ diffusion, rather than glutamate diffusion, as the leading event in cortical spreading depression.

Key words: Astrocytes, calcium, glutamate, migraine, potassium

Introduction

Cortical spreading depression (CSD), discovered by Aristides Leão in 1944 (Leão 1944), and hypoxic CSD-like depolarization represent a catastrophic failure of the brain's ion, volume, and neurotransmitter homeostatic machinery (Somjen 2001; Sykova and Nicholson 2008; Pietrobon and Moskowitz 2014). Accumulating evidence indicates that the phenomenon is associated with migraine headache, stroke, traumatic brain injury, and subarachnoid hemorrhage (Takano and Nedergaard 2009; Dreier 2011;

Charles and Baca 2013). Decades of research have revealed the excitotoxic nature of the condition, and implicated Ca^{2+} (Leibowitz 1992; Herreras et al. 1994; Nedergaard 1994), K^+ (Grafstein 1956; Vyskocil et al. 1972), and glutamate waves (Van Harreveld 1959; Fabricius et al. 1993). However, microscopic investigation of the precise localization and timing of such events, critical for understanding the molecular basis of CSD, have been hampered by the lack of specific, sensitive, high-resolution and fast methods to detect these transients in living animals. We took advantage of recently developed, genetically encoded fluorescent indicators for Ca^{2+} (Chen et al. 2013) and glutamate (Marvin et al. 2013) for high-speed, micrometer spatial resolution, 2-photon imaging in combination with electrophysiology to identify the precise order of ionic shift dynamics at the CSD wavefront.

Materials and Methods

Animals

Male C57BL/6N mice of at least 10 weeks of age (Charles River) were used for the experiments. The mice were housed on a 12-h light:12-h dark cycle (lights on at 8 AM), 1–4 mice per cage. All experimental groups contain at least 4 animals, which is in line with sample sizes in the literature. Adequate measures were taken to minimize pain and discomfort. Experiments were carried out in accordance with the guidelines published in the European Communities Council Directive of 24. November 1986 (86/609/EEC). All procedures were approved by the Animal Use and Care Committee of the Institute of Basic Medical Sciences, The Faculty of Medicine, University of Oslo.

Plasmid Constructs

The genetically encoded fluorescent Ca^{2+} indicator GCaMP6f (Chen et al. 2013) DNA sequence was amplified by PCR from pGP-CMV-GCaMP6f (Addgene) with BamHI and HindIII at the 5′ and 3′ ends, respectively, and sub-cloned into the recombinant adeno-associated virus (rAAV) vector pAAV-6P-SEWB (Shevtsova et al. 2005), with the human synapsin-1 (SYN) promoter to generate the construct pAAV-SYN-GCaMP6f. The human glial fibrillary acidic protein (GFAP) promoter (Hirrlinger et al. 2009) was inserted with MluI and BamHI into pAAV-SYN-GCaMP6f, resulting in the pAAV-GFAP-GCaMP6f construct. Virus from pAAV-SYN-iGluSnFR (Marvin et al. 2013) was used to express the genetically encoded fluorescent glutamate indicator iGluSnFR in neurons.

Virus Transduction

rAAVs serotype 1 and 2 were generated as described (Tang et al. 2009), and purified by AVB Sepharose affinity chromatography (Smith et al. 2009). For each virus preparation, the genomic titer was determined by Real-Time PCR ($1.0–6.0 \times 10^{12}$ viral genomes (vg)/ml, TaqMan Assay, Applied Biosystems). For adult infections, the mice were deeply anesthetized with a mixture of zolazepam (188 mg/kg body weight), tiletamine (188 mg/kg body weight), xylazine (4.5 mg/kg body weight) and fentanyl (26 µg/kg body weight) before viruses were stereotactically injected (Shevtsova et al. 2005). For injections in visual cortex, stereotactic coordinates relative to Bregma were: anteroposterior −3.0 mm, lateral +2.5 mm, and depth 0.4 mm. During each injection, 0.3 µl of purified rAAVs was delivered.

Immunohistochemistry and Confocal Imaging

Mice were anesthetized with ~4% isoflurane and intracardially perfused with phosphate buffered saline (PBS; 137 mM NaCl, 2.7 mM KCl, 4.3 mM $Na_2HPO_4/2H_2O$, 1.4 mM KH_2PO_4, pH 7.4, all from Sigma-Aldrich) and 4% paraformaldehyde (PFA, Merck) prior to decapitation. Brains were removed and fixed in ice-cold 4% PFA/PBS for 2 h and sliced on a vibratome (Leica) into 70 µm sections. Immunostaining was performed with polyclonal rabbit anti-GFP (1:3000, Abcam, #ab6556), chicken anti-GFAP (1:1000, Covance, #PCK-591P), and FITC-coupled anti-rabbit and Cy3-coupled anti-chicken secondary antibodies (1:200, Jackson Immuno Research, #711095152 and #703165155, respectively). Confocal images were acquired on a Zeiss LSM5 PASCAL confocal laser scanning microscope with 10x/0.45NA and 63×/1.4NA oil-immersion objective, equipped with an Argon laser (457, 476, 488, 514 nm) and a Helium Neon laser (543 nm, Carl Zeiss). Image analysis was done with ImageJ (v10.2, NIH).

Surgical Procedures and Induction of CSD

Anesthesia was induced in a chamber containing 4% isoflurane in room air enriched with 20% pure oxygen, and subsequently maintained by nose cone flowing 2% isoflurane. Body temperature was monitored with a rectal probe and kept at 37°C by a temperature-controlled heating pad. Buprenorphine 0.15 mg/kg was injected intraperitoneally and the mice were left for 10 min before surgery started. We then performed a tracheotomy and artificially ventilated the mice with a mixture of isoflurane (2% for surgical procedures, 1.5% during imaging) in room air with a small animal ventilator (SAR-1000; CWE Inc.). The left femoral artery was cannulated for analyses of arterial blood gas values and the ventilator settings were adjusted to maintain physiological values ($pO_2 = 80–120$ mmHg, $pCO_2 = 25–35$ mmHg, pH = 7.30–7.50). An intravenous catheter was inserted in the femoral vein to enable injection of Texas Red-labeled dextran (Life Technologies) for visualization of the vasculature.

A 2 mm craniotomy with center coordinates anteroposterior −3.0 mm, lateral + 2.5 mm relative to Bregma was created as previously described (Takano et al. 2006). In short, a dental drill was used to carefully carve a circular groove in the skull with intermittent application of saline for cooling and removal of debris until only approximately 0.1 mm of the bone thickness was left. The skull was then soaked for 10 min to soften before the bone flap was removed. Subsequently, the dura was carefully removed with a vessel dilator under saline. Agarose (0.8%) in saline was applied to the brain's surface and stabilized with a cover slip. The cover slip covered ~80% of the craniotomy to enable insertion of an extracellular electrode. Furthermore, a small secondary craniotomy was made approximately 4 mm rostral to the imaging window to allow epidural application of KCl (1.5–2 µl, 1 M) for induction of CSD waves. The small droplet of KCl was left for the duration of one imaging trial. The rostral craniotomy was subsequently rinsed in saline and left bathed in saline until the next CSD wave was elicited. In experiments with K^+-sensitive microelectrodes, 1.1% agarose in saline was used and no cover slip was added.

Electrophysiology

Glass electrodes of 2–5 MΩ impedance were filled with physiological saline (154 mM NaCl) and inserted into the cortex between the edge of the cover glass and the edge of the craniotomy in the imaging window to record direct current (DC) shifts accompanying CSD waves. In a subset of experiments the tip of the glass electrode was filled with 250 µg/ml Texas Red-labeled dextran (Life Technologies) in physiological saline to enable 2-photon visualization of the electrode. A corresponding DC shift was identified in all trials and subsequently analyzed in MATLAB (R2013b, MathWorks, Inc.).

For $[K^+]_e$ measurements, ion-sensitive microelectrodes with tip sizes of approximately 3 μm were silanized with gaseous N,N-dimethyltrimethylsilylamine (41 716, Sigma-Aldrich) at 200°C for approximately 20 min and then filled with 150 mM NaCl and 3 mM KCl (Voipio et al. 1994). The tips of the electrodes were filled with a liquid K^+ ion exchanger (IE190; World Precision Instruments) by gentle suction. Before imaging, the electrodes were calibrated by standard solutions of known K^+ concentration (3, 10, 25, 50, and 75 mM). Signal from the reference microelectrode was subtracted from that of the ion-sensitive microelectrode to get a signal that reflects only the $[K^+]_e$. A log-linear fit was used to calculate the actual $[K^+]_e$ in each experiment. The K^+-sensitive microelectrode and an extracellular reference electrode were positioned so that their tips were as close as possible (max 50 μm). All electrophysiological recordings were done with Multiclamp 700B with headstage CV-7B for extracellular recordings and CV-7B/EC for $[K^+]_e$ measurement. Signals were digitized by Digidata 1440 and further analyzed by pCLAMP 10.4 (all from Molecular Devices, LLC). A threshold of 0.25 mM $[K^+]_e$ increase from baseline was used to identify the starting point of the $[K^+]_e$ increase.

Two-photon Microscopy

GCaMP6f or iGluSnFR fluorescence was recorded by a 2-photon laser scanning microscope (model "Ultima", Prairie Technologies). Images were recorded from cortical layers 2/3 with a model "XLPLN 25 × WMP" 1.05NA, water-immersion objective (Olympus), using 900–910 nm laser pulses for excitation with an average power of 6–14 mW, as measured by LaserCheck (Coherent). The laser was a model "Mai Tai DeepSee" (Spectra Physics). Time-series and electrophysiological recordings were triggered by pCLAMP 10.4 (Molecular Devices, LLC) to enable precise timing of the DC shifts and corresponding images. Most time-series were performed with frame rates of approximately 4 Hz, but a subset of experiments was performed with 1 or 6 Hz acquisition rates.

Image Analysis

Time-series of fluorescence images were imported into Fiji ImageJ (Fiji), and regions of interest (ROIs) were manually selected based on morphology.

In rAAV-$GFAP$-GCaMP6f injected mice ROIs defining astrocytic compartments were carefully selected over somata, processes and endfeet of cells with typical astrocyte morphology. The relative change in mean fluorescence (ΔF/F) over time was calculated in each ROI and subsequently analyzed by custom-written MATLAB scripts (R2013b, MathWorks, Inc.). Mean plus 2 standard deviations of the baseline (first 30 s) was used to identify fluorescent events.

Statistics

Statistical analyses were performed using Prism (Version 6.0b for Mac OSX, GraphPad Software). Unless stated otherwise, all values are given as mean and standard error of the mean (SEM). One-way ANOVA with Tukey multiple comparisons tests was used for comparisons between timing of the different fluorescent probes to the DC shift and duration of Ca^{2+} signals in astrocyte subcompartments as well as wave speed with different fluorophores. The data passed the D'Agostino and Pearson omnibus normality test, and Bartlett's homogeneity of variances test. For the rest of the analyses, 2-sided Student's t-test was used as frequency distribution histograms displayed a normal distribution pattern.

Results

First GCaMP6f, expressed in neurons by rAAV delivery using the human synapsin (SYN) promoter, was used to follow neuronal $[Ca^{2+}]_i$ while DC potential was measured with an extracellular recording electrode. CSD events were initiated through focal epidural application of KCl in a separate, distant craniotomy and tracked by imaging through a cranial window and electrophysiology (Fig. 1A). Electrically recorded CSD events were associated with strong increases in GCaMP6f fluorescence in visual cortex layer 2/3 pyramidal neurons, moving as waves across the field of view with speeds of 56.7 ± 3.3 μm/s ($n = 28$ waves, 11 mice, SEM; Fig. 1B,C and Supplementary Movie 1). Wavefronts were sharp with no apparent lag between the Ca^{2+} rises in somata and processes (Fig. 1B). The Ca^{2+} transients also had similar amplitudes in the 2 compartments, but lasted significantly longer in somata than in processes (Fig. 1D).

The neuronal Ca^{2+} transients lasted approximately twice as long as the negative DC potential shift, which persisted for 66.4 ± 3.8 s ($n = 24$ waves, 10 mice). Neuronal GCaMP6f fluorescence returned to baseline more quickly in the vicinity of penetrating arterioles (Fig. 1B, 50 s image). The transient tissue boundaries of GCaMP6f fluorescence in the recovery phase exhibited remarkably delineated circular patterns resembling those of NADH fluorescence in metabolically stressed cortical tissue (Takano et al. 2007; Kasischke et al. 2011). The shorter duration of neuronal Ca^{2+} transients in peri-arteriolar tissue (Fig. 1E) may depend on faster recovery from metabolic dysfunction due to ready oxygenation (Sakadzic et al. 2010; Kasischke et al. 2011; Yaseen et al. 2011). In support of this hypothesis, the radius of the tissue cylinder with rapidly recovering Ca^{2+} levels directly correlated with arteriolar diameter (Fig. 1F).

In ~15% of experiments ($n = 42$ waves, 13 mice) one or a few neurons exhibited Ca^{2+} spikes in front of the approaching neuronal Ca^{2+} wave (Fig. 1G). These spikes preceded the Ca^{2+} wave by ~30 μm (~0.5 s) and may represent prodromal spike bursts (Herreras et al. 1994). We next performed imaging at 4–6 Hz in cortical layer 2/3 for increased temporal resolution at the wavefront. The latency between the onset of the negative DC potential shift and the neuronal Ca^{2+} increase was 1.1 ± 0.1 s ($n = 22$ waves, 9 mice; Fig. 1H,I), indicating that neuronal Ca^{2+} signals are not leading events in CSD propagation.

What about the astrocytic Ca^{2+} waves in CSD? Due to the comparable kinetics of CSD waves and astrocytic Ca^{2+} waves, the latter have been proposed to play a role in CSD propagation (Leibowitz 1992). Here we used the human glial fibrillary acidic protein ($GFAP$) promoter to drive GCaMP6f expression in astrocytes. Immunofluorescence confirmed expression of GCaMP6f in astrocytes, while the vast majority of cortical neurons were immunonegative (Fig. 2).

Similarly to neurons, GCaMP6f expressing astrocytes exhibited KCl-induced Ca^{2+} waves that spread at a speed of 55.7 ± 1.7 μm/s ($n = 28$ waves, 9 mice; Fig. 3A,B and Supplementary Movie 2). The astrocytic Ca^{2+} wavefront was not as regular as the neuronal Ca^{2+} wavefront, yet there was no apparent lag between somata, processes, and endfeet. The amplitude of the Ca^{2+} increase was comparable in all astrocytic compartments, whereas the duration was somewhat longer in endfeet than in somata (Fig. 3C). Strikingly, the Ca^{2+} transients in astrocytic somata, processes and endfeet were shorter than those in neuronal somata and processes (40.7 ± 2.1 s, 44.7 ± 2.4 s and 50.5 ± 2.1 s vs. 170.6 ± 12.9 s and 132.7 ± 13.0 s, respectively, $P < 0.05$ for all comparisons, One-way ANOVA with Tukey multiple comparisons test; Figs 1D and 3C), returning to baseline before DC potential recovery.
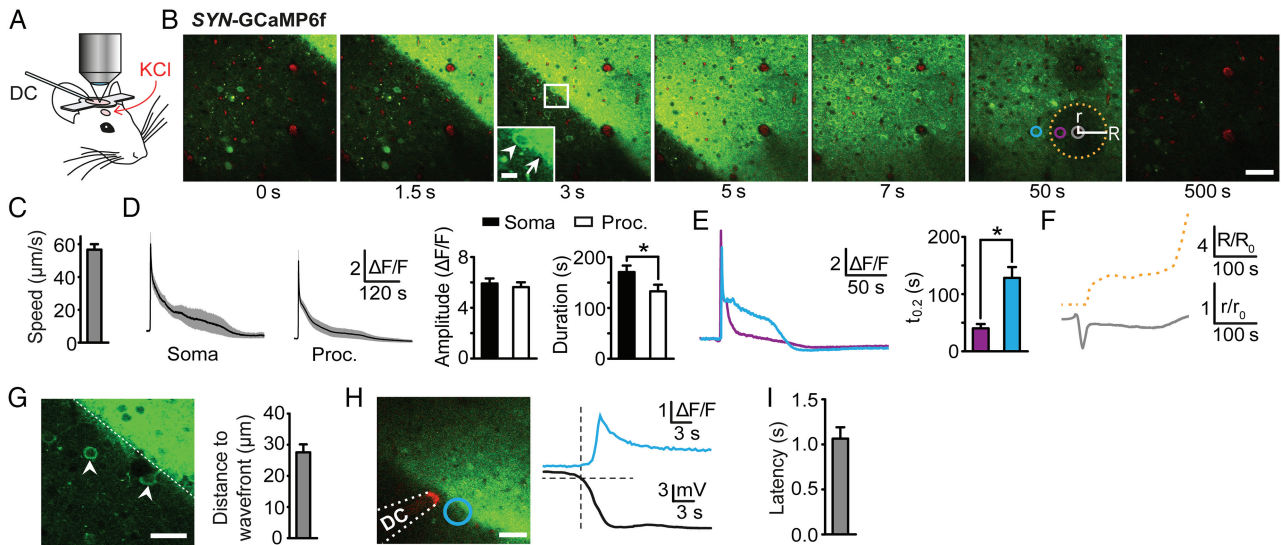
Figure 1. [Ca^{2+}]$_i$ dynamics in visual cortex layer 2/3 neurons during CSD. (A) Experimental setup. (B) Neuronal GCaMP6f fluorescence (green) during passage of a CSD wave. Blood vessels are outlined with Texas Red. Inset in 3 s image is boxed region and shows the involvement of both neuronal somata (arrowhead) and processes (arrow) in the advancing Ca^{2+} wavefront. Neuronal Ca^{2+} levels recovered faster in the vicinity of arterioles (cf. image at 50 s). (C) Speed of the neuronal Ca^{2+} wave. (D) Average fluorescence traces (with 95% confidence interval shown in gray), amplitude, and duration of Ca^{2+} transients in neuronal somata ($n = 46$ cells, 13 waves, 10 mice) and processes ($n = 59$ cells, 21 waves, 11 mice). (E) Representative traces from regions of interest as indicated in (B) (50 s image), 25 μm (violet) and 50 μm (blue) from the center of an arteriole, and 20% width of transient in similar regions of interest ($n = 9$ waves, 7 mice). (F) The radius (R) of the tissue cylinder with pre-CSD Ca^{2+} levels (yellow dotted line) varied with the arteriolar diameter changes (r; gray trace). (G) In 15% of the recordings ($n = 42$ waves, 13 mice), discrete neurons (arrowheads) were excited in front of the main Ca^{2+} wave (dashed line). Bar graph with average distance from neurons to the main Ca^{2+} wavefront ($n = 7$ waves, 7 mice). (H) (Left) Image of GCaMP6f fluorescence close to the tip of the DC potential electrode. Blue circle indicates sampled area, aligned to the wave front as it reaches the tip of the DC electrode. (Right) Neuronal Ca^{2+} (blue trace) and DC potential (black trace). (I) Latency between negative DC deflection and neuronal [Ca^{2+}]$_i$ increase. Scale bars: 50 (B), 10 (B, inset), and 25 (G, H) μm. *$P < 0.05$; error bars, SEM.
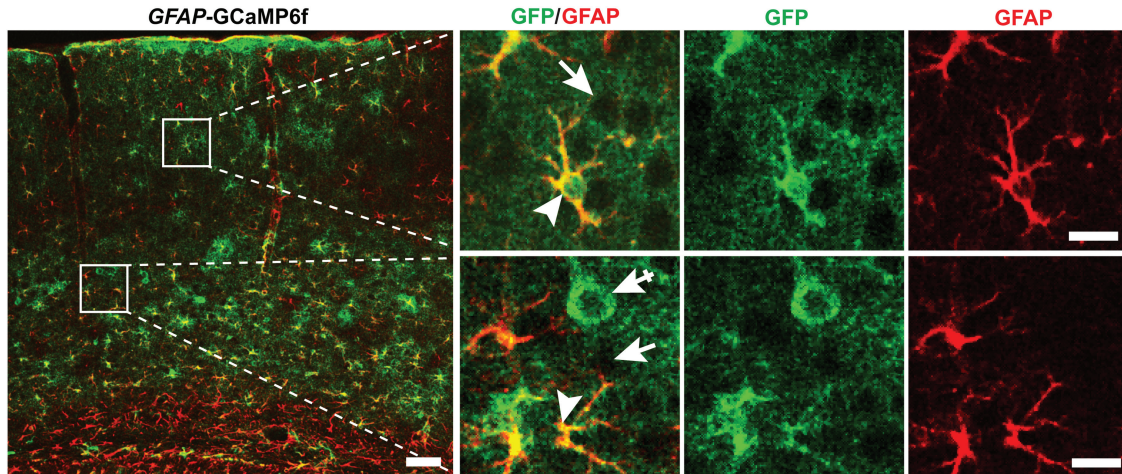
Figure 2. Immunofluorescence micrographs from mouse brain injected with rAAV-*GFAP*-GCaMP6f. (Left) Overview image of a coronal cortical section stained with antibodies against GFP (green, visualized with FITC-coupled antibody) and GFAP (red, visualized with Cy3-coupled antibody). Scale bar: 100 μm. (Right) higher magnification images of boxed regions in layer 2/3 and layer 4/5. GFAP-immunopositive astrocytes (arrowheads) express GCaMP6f (GFP antibody, green), while the majority of neuronal cell bodies are immunonegative (arrows). Sparse neuronal GFP labeling was noted (crossed arrow), mainly in layer 4/5. Scale bars: 10 μm.

Recovery of astrocytic GCaMP6f fluorescence occurred without microregional differences, as observed for the neuronal GCaMP6f fluorescence.

Imaging at 4–6 Hz revealed that the latency between the onset of the negative DC potential shift and the astrocytic Ca^{2+} increase was 4.0 s ± 0.2 s ($n = 19$ waves, 7 mice; Fig. 3D,E), significantly longer than the corresponding neuronal latency ($P < 0.0001$, Student's t-test). The delayed onset of astrocytic versus neuronal Ca^{2+} transients was also confirmed in mice expressing GCaMP6f in

neurons and GCaMP6f together with the red fluorescent reporter tdTomato in astrocytes (Fig. 3F).

Using subcellular-resolution 2-photon imaging we assessed the relationship between endfoot Ca^{2+} levels and diameter changes of intracortical arterioles. The arteriolar response to CSD was variable and multiphasic, as reported previously (Charles and Baca 2013), with an initial dilation, a constriction, a delayed dilation and a delayed, long-lasting constriction. The endfoot Ca^{2+} increase was consistently followed by arteriolar
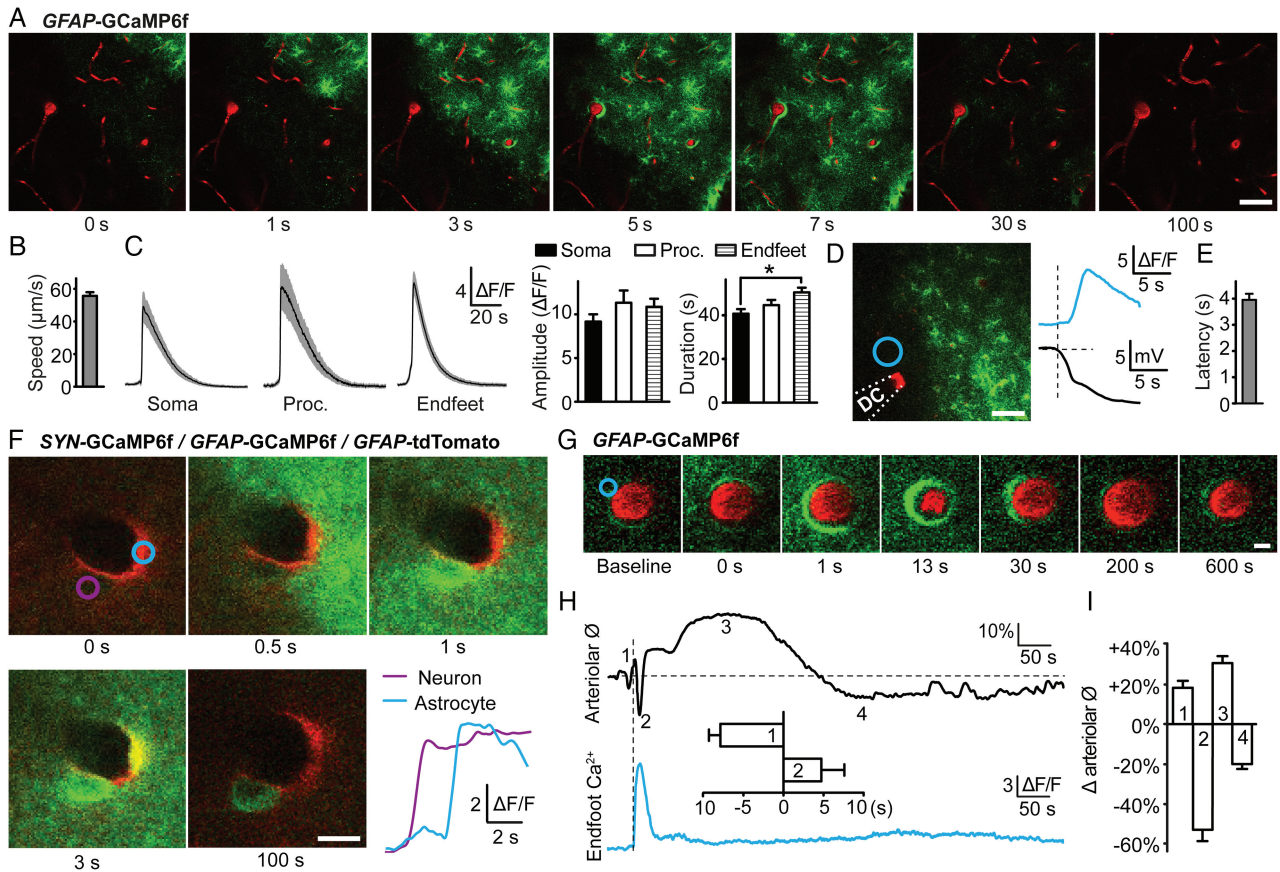
Figure 3. $[Ca^{2+}]_i$ dynamics in astrocytes during CSD. (A) As in Figure 1B, but with GCaMP6f expressed in astrocytes. (B) Speed of the astrocytic Ca^{2+} wave. (C) Average fluorescence traces (with 95% confidence interval shown in gray), amplitude, and duration (soma: $n = 44$ cells, 17 waves, 9 mice; large processes: $n = 14$ cells, 11 waves, 6 mice; endfeet: $n = 45$ cells, 20 waves, 9 mice) of Ca^{2+} transients in astrocytic compartments. (D) (Left) Image of GCaMP6f fluorescence close to the tip of the DC potential electrode. Blue circle indicates sampled area, aligned to the wave front as it reaches the tip of the DC electrode. (Right) Astrocytic Ca^{2+} trace aligned to the DC potential. (E) Latency between negative DC deflection and astrocytic $[Ca^{2+}]_i$ increase. (F) Dual-channel imaging of mice cotransduced with rAAV-SYN-GCaMP6f, rAAV-GFAP-GCaMP6f, and rAAV-GFAP-tdTomato reveals the timing of the $[Ca^{2+}]_i$ increase in a neuronal cell body (purple circle) and a nearby astrocytic endfoot (with tdTomato; blue circle) during CSD. Representative GCaMP6f fluorescence traces from regions of interest as indicated in the image. (G) Sequence of images of a penetrating arteriole (outlined with Texas Red) and GCaMP6f fluorescence (green) in a peri-arteriolar astrocytic endfoot during CSD. 0 s defined as the first notable endfoot Ca^{2+} increase. (H) Diameter changes of the vessel in (G) (top), aligned to the fluorescence trace from the endfoot (bottom). The arteriolar response to CSD had 4 discernable phases: an initial dilation, a constriction, a delayed dilation and a delayed, prolonged constriction. All phases were present in 29 of 54 vessels (53.7%) analyzed. Numbers 1–4 indicate the peaks of the initial vasodilation, the consecutive constriction, the delayed dilation, and the delayed, long-lasting constriction, respectively. The bar diagram between the traces shows the temporal relationship between the endfoot $[Ca^{2+}]_i$ rise (time = 0 s) and the first 2 arteriolar phases. Endfoot $[Ca^{2+}]_i$ increase starts 7.9 ± 1.4 s after onset of the initial dilation ($n = 7$ waves, 7 mice), and is followed by constriction after 4.7 ± 2.9 s ($n = 14$ waves, 14 mice). (I) Average amplitudes of the diameter changes at peaks 1 ($n = 39$ waves, 15 mice), 2 ($n = 39$ waves, 15 mice), 3 ($n = 32$ waves, 12 mice), and 4 ($n = 29$ waves, 10 mice) indicated in (H). Scale bars: 50 μm (A,D) and 10 μm (F,G). *$P < 0.05$; error bars, SEM.

constriction ($n = 14$ waves, 14 mice; Fig. 3G–I and Supplementary Movie 3), in line with data obtained in immature rats (Chuquet et al. 2007). Notably, neither the subsequent dilation nor the delayed constriction coincided with endfoot Ca^{2+} transients.

Since the negative DC potential shift preceded Ca^{2+} rises in both neurons and astrocytes, we went on to assess the dynamics of extracellular glutamate levels in CSD. Using the glutamate indicator iGluSnFR (Marvin et al. 2013) expressed on the external surface of neurons, we found that CSD was accompanied by a wave of increased $[glutamate]_e$ (Fig. 4A and Supplementary Movie 4), as previously shown by microdialysis (Fabricius et al. 1993). The glutamate increase traveled at 51.7 ± 0.3 μm/s ($n = 28$ waves, 6 mice; Fig. 4B), not significantly different from the speed of the Ca^{2+} waves in neurons and glia ($P = 0.33$ and $P = 0.20$, respectively, One-way ANOVA with Tukey multiple comparisons test), and lasted only 18.6 ± 1.7 s ($n = 12$ waves, 4 mice; Fig. 4C). Higher speed (4–6 Hz) imaging revealed that the

increase in iGluSnFR fluorescence passed the tip of the DC electrode 1.9 ± 0.2 s after the negative DC deflection ($n = 29$ waves, 8 mice; Fig. 4D,E), significantly different from the GCaMP6f latency in neurons and astrocytes ($P = 0.0002$ and $P < 0.0001$, respectively, One-way ANOVA with Tukey multiple comparisons test). Thus, extracellular glutamate levels increased after passage of the neuronal Ca^{2+} wavefront, but before the arrival of the astrocytic Ca^{2+} wave.

Finally, we measured the lag between CSD-associated $[K^+]_e$ rise (defined as 0.25 mM above baseline levels and measured by K^+-sensitive microelectrodes), and increases in neuronal GCaMP6f fluorescence (Fig. 4F), astrocytic GCaMP6f fluorescence (Fig. 4G), and iGluSnFR fluorescence (Fig. 4H). The $[K^+]_e$ rise preceded negative DC deflection, neuronal Ca^{2+} increase, extracellular glutamate increase and astrocytic Ca^{2+} increase by 5.9 ± 0.4 s ($n = 41$ waves, 10 mice), 6.2 ± 0.6 s ($n = 13$ waves, 4 mice), 7.7 ± 0.7 s ($n = 19$ waves, 4 mice) and 9.3 ± 0.7 s ($n = 11$ waves, 3 mice),
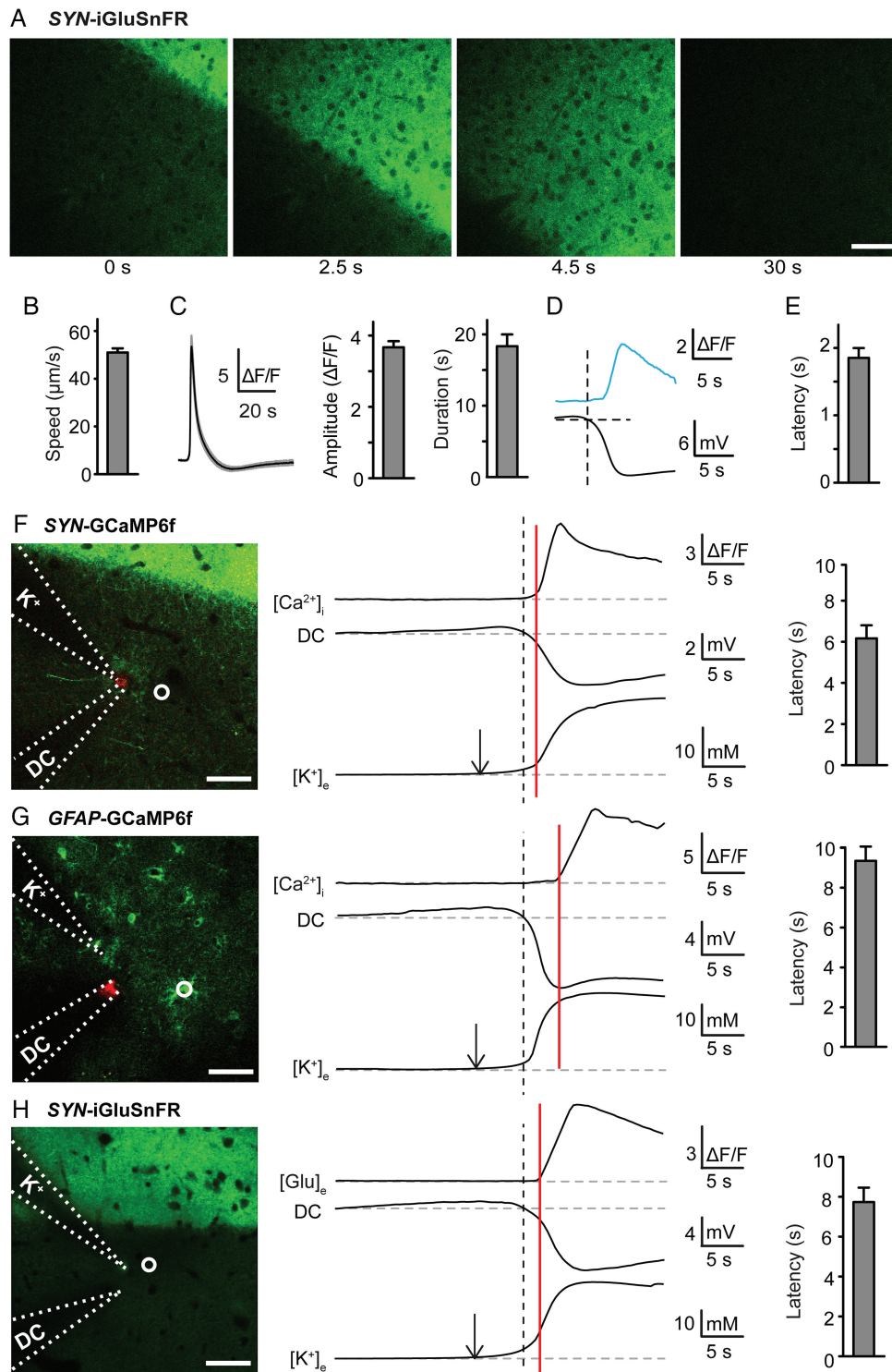
Figure 4. Dynamics of extracellular glutamate and K+ in CSD. (A) As in Figure 1A, but with iGluSnFR to reveal extracellular glutamate levels. (B) Speed of the extracellular glutamate wave. (C) Average fluorescence traces with 95% confidence interval, amplitude, and duration of the glutamate transient. (D) Glutamate trace aligned to the DC potential. (E) Latency between negative DC deflection and glutamate increase. (F) Relationship between $[K^+]_e$, DC potential, and neuronal $[Ca^{2+}]_i$. The latency between 0.25 mM $[K^+]_e$ rise (arrow over K+ trace) and increase in fluorescence (red vertical line) is indicated to the right. Dashed line indicates start of the negative DC potential shift. (G) As in (F) but with $[Ca^{2+}]_i$ in astrocytes instead of neurons. (H) As in (F) but with $[glutamate]_e$ instead of neuronal $[Ca^{2+}]_i$. Images in (F–H) show positions of electrodes (stippled lines) and sampled regions (white circles). Sampled regions were picked along the front edge of the CSD wave as it hit the potassium sensitive microelectrode. Scale bars: 50 μm; error bars, SEM.

respectively (Fig. 4F–H). Further analysis revealed that $[K^+]_e$ had reached 7.3 ± 0.6 mM when the neuronal Ca^{2+} wavefront hit the tip of the K+-sensitive microelectrode. Thus, our data clearly show that an interstitial K+ surge is ahead of the advancing CSD wave and may reach levels sufficient to induce a substantial neuronal depolarization.

Discussion

It is widely accepted that CSD involves a regenerative cycle of neuronal depolarization, release of K^+ and glutamate and further depolarization that spreads in a wave-like manner at velocities several orders of magnitude slower than that of action potentials in even the smallest unmyelinated axons or dendrites (Andersen et al. 1978; Buzsaki and Kandel 1998; Somjen 2001). Activation of voltage-gated Na^+ channels, voltage-gated Ca^{2+} channels, and N-methyl-D-aspartate (NMDA) ionotropic glutamate receptors is thought to be involved in the positive feedback cycle of depolarizing inward currents during CSD ignition, yet the relative contribution of these inward currents during the course of the CSD wave is unknown (Somjen 2001; Pietrobon and Moskowitz 2014). Our finding that the neuronal $[Ca^{2+}]_i$ rise precedes the interstitial glutamate surge suggests that neuronal voltage-activated currents, and not glutamate-mediated NMDA receptor currents, are initiating the vicious cycle of neuronal depolarization and release of K^+ and glutamate. Thus, our data do not lend support to van Harreveld's idea that interstitial glutamate diffusion carries the CSD wave (Van Harreveld 1959). However, as $[glutamate]_e$ increased ahead of the astrocytic $[Ca^{2+}]_i$ rise, the latter is likely attributable to interstitial glutamate acting through metabotropic glutamate receptor activation.

The later passage of astrocytic than neuronal Ca^{2+} waves further argues against a role of astrocytes in propagating CSD, an idea first proposed 2 decades ago due to the similar temporal and spatial characteristics of astrocytic Ca^{2+} waves and CSD (Leibowitz 1992). This concept is also challenged by the finding that pharmacological inhibition of astrocytic Ca^{2+} signaling does not prevent propagation of the CSD wave (Peters et al. 2003; Chuquet et al. 2007). Neither did we find support for the idea that neuronal Ca^{2+} influx triggered by intercellular current flow between gap junction-coupled neurons is the primary driver of CSD (Herreras et al. 1994). The combined use of K^+-sensitive microelectrodes and 2-photon calcium imaging clearly showed that neuronal Ca^{2+} signals lagged behind interstitial K^+ elevation.

Lack of tools to map rapid changes in ion and neurotransmitter levels in the adult brain with sub-cellular resolution has delayed progress in understanding mechanisms underlying CSD. Microdialysis and enzyme-based measurements of interstitial glutamate do not offer sufficient spatiotemporal resolution to determine the timing of the glutamate surge in relation to the CSD wavefront. The vast majority of Ca^{2+} imaging studies on CSD have employed bulk loading of synthetic Ca^{2+} indicators (Peters et al. 2003; Chuquet et al. 2007), a strategy with low efficacy in adult animals and poor sensitivity for detecting Ca^{2+} signals in distal cellular processes (Reeves et al. 2011). These shortcomings notwithstanding, Ca^{2+} imaging data obtained in immature rats indicated that CSD-associated Ca^{2+} waves appear in neurons before astrocytes (Chuquet et al. 2007), in line with our GCaMP6f fluorescence data in adult mice.

Our finding that CSD-associated Ca^{2+} transients last significantly longer in neuronal somata than in processes contrasts data obtained in acute hippocampal slices, where $[Ca^{2+}]_i$ in CA1 pyramidal cells (measured by patch pipette delivery of the low-affinity ratiometric Ca^{2+} indicator Fura-6F) was elevated for significantly longer in dendrites (Aiba and Shuttleworth 2012). This discrepancy may hinge on altered function of patched cells (whose contents are dialyzed with the pipette solution), on differences between cortical and hippocampal neurons, or on differences between the in vivo situation and the slice preparation, for example, due to altered metabolism or network connectivity/activity.

The present study was performed in isoflurane-anesthetized animals. Isoflurane has been shown to influence CSD susceptibility and propagation speed in a dose-dependent manner, but not DC shift amplitudes and durations (Kitahara et al. 2001; Kudo et al. 2013). Nonetheless, CSD was readily elicited in our model and the waves we observed had similar propagation velocity as previously reported in number of animal models in vitro and in vivo (Somjen 2001) and in the awake human visual cortex (Hadjikhani et al. 2001).

To our knowledge, correlation of cellular Ca^{2+} signals with interstitial surges of potassium and glutamate in CSD has not been studied previously. Development of optical probes for other ions and signaling molecules will further advance our understanding of the complex phenomena of CSD and related spreading depolarizations, and likely pave the way for more effective treatment of migraine and other conditions. The data here already point towards K^+ flooding into the interstitial space as the lynchpin of these events.

Supplementary Material

Supplementary material can be found at: http://www.cercor.oxfordjournals.org/.

Notes

Conflict of Interest: None declared.

References

Aiba I, Shuttleworth CW. 2012. Sustained NMDA receptor activation by spreading depolarizations can initiate excitotoxic injury in metabolically compromised neurons. J Physiol. 590:5877–5893.

Andersen P, Silfvenius H, Sundberg SH, Sveen O, Wigstrom H. 1978. Functional characteristics of unmyelinated fibres in the hippocampal cortex. Brain Res. 144:11–18.

Buzsaki G, Kandel A. 1998. Somadendritic backpropagation of action potentials in cortical pyramidal cells of the awake rat. J Neurophysiol. 79:1587–1591.

Charles AC, Baca SM. 2013. Cortical spreading depression and migraine. Nat Rev Neurol. 9:637–644.

Chen TW, Wardill TJ, Sun Y, Pulver SR, Renninger SL, Baohan A, Schreiter ER, Kerr RA, Orger MB, Jayaraman V, et al. 2013. Ultrasensitive fluorescent proteins for imaging neuronal activity. Nature. 499:295–300.

Chuquet J, Hollender L, Nimchinsky EA. 2007. High-resolution in vivo imaging of the neurovascular unit during spreading depression. J Neurosci. 27:4036–4044.

Dreier JP. 2011. The role of spreading depression, spreading depolarization and spreading ischemia in neurological disease. Nat Med. 17:439–447.

Fabricius M, Jensen LH, Lauritzen M. 1993. Microdialysis of interstitial amino acids during spreading depression and anoxic depolarization in rat neocortex. Brain Res. 612:61–69.

Grafstein B. 1956. Mechanism of spreading cortical depression. J Neurophysiol. 19:154–171.

Hadjikhani N, Sanchez Del Rio M, Wu O, Schwartz D, Bakker D, Fischl B, Kwong KK, Cutrer FM, Rosen BR, Tootell RB, et al. 2001. Mechanisms of migraine aura revealed by functional MRI in human visual cortex. Proc Natl Acad Sci USA. 98: 4687–4692.

Herreras O, Largo C, Ibarz JM, Somjen GG, Martin del Rio R. 1994. Role of neuronal synchronizing mechanisms in the propagation of spreading depression in the in vivo hippocampus. J Neurosci. 14:7087–7098.

Hirrlinger J, Scheller A, Hirrlinger PG, Kellert B, Tang W, Wehr MC, Goebbels S, Reichenbach A, Sprengel R, Rossner MJ, et al. 2009. Split-cre complementation indicates coincident activity of different genes in vivo. PloS One. 4:e4286.

Kasischke KA, Lambert EM, Panepento B, Sun A, Gelbard HA, Burgess RW, Foster TH, Nedergaard M. 2011. Two-photon NADH imaging exposes boundaries of oxygen diffusion in cortical vascular supply regions. J Cereb Blood Flow Metab. 31:68–81.

Kitahara Y, Taga K, Abe H, Shimoji K. 2001. The effects of anesthetics on cortical spreading depression elicitation and c-fos expression in rats. J Neurosurg Anesthesiol. 13:26–32.

Kudo C, Toyama M, Boku A, Hanamoto H, Morimoto Y, Sugimura M, Niwa H. 2013. Anesthetic effects on susceptibility to cortical spreading depression. Neuropharmacology. 67:32–36.

Leão AAP. 1944. Spreading depression of activity in the cerebral cortex. J Neurophysiol. 7:359–390.

Leibowitz DH. 1992. The glial spike theory. I. On an active role of neuroglia in spreading depression and migraine. Proc Biol Sci. 250:287–295.

Marvin JS, Borghuis BG, Tian L, Cichon J, Harnett MT, Akerboom J, Gordus A, Renninger SL, Chen TW, Bargmann CI, et al. 2013. An optimized fluorescent probe for visualizing glutamate neurotransmission. Nat Methods. 10:162–170.

Nedergaard M. 1994. Direct signaling from astrocytes to neurons in cultures of mammalian brain cells. Science. 263:1768–1771.

Peters O, Schipke CG, Hashimoto Y, Kettenmann H. 2003. Different mechanisms promote astrocyte Ca2+ waves and spreading depression in the mouse neocortex. J Neurosci. 23: 9888–9896.

Pietrobon D, Moskowitz MA. 2014. Chaos and commotion in the wake of cortical spreading depression and spreading depolarizations. Nat Rev Neurosci. 15:379–393.

Reeves AM, Shigetomi E, Khakh BS. 2011. Bulk loading of calcium indicator dyes to study astrocyte physiology: key limitations and improvements using morphological maps. J Neurosci. 31:9353–9358.

Sakadzic S, Roussakis E, Yaseen MA, Mandeville ET, Srinivasan VJ, Arai K, Ruvinskaya S, Devor A, Lo EH, Vinogradov SA, et al. 2010. Two-photon high-resolution measurement of partial pressure of oxygen in cerebral vasculature and tissue. Nat Methods. 7:755–759.

Shevtsova Z, Malik JM, Michel U, Bahr M, Kugler S. 2005. Promoters and serotypes: targeting of adeno-associated virus vectors for gene transfer in the rat central nervous system in vitro and in vivo. Exp Physiol. 90:53–59.

Smith RH, Levy JR, Kotin RM. 2009. A simplified baculovirus-AAV expression vector system coupled with one-step affinity purification yields high-titer rAAV stocks from insect cells. Mol Ther. 17:1888–1896.

Somjen GG. 2001. Mechanisms of spreading depression and hypoxic spreading depression-like depolarization. Physiol Rev. 81:1065–1096.

Sykova E, Nicholson C. 2008. Diffusion in brain extracellular space. Physiol Rev. 88:1277–1340.

Takano T, Nedergaard M. 2009. Deciphering migraine. J Clin Invest. 119:16–19.

Takano T, Tian GF, Peng W, Lou N, Libionka W, Han X, Nedergaard M. 2006. Astrocyte-mediated control of cerebral blood flow. Nat Neurosci. 9:260–267.

Takano T, Tian GF, Peng W, Lou N, Lovatt D, Hansen AJ, Kasischke KA, Nedergaard M. 2007. Cortical spreading depression causes and coincides with tissue hypoxia. Nat Neurosci. 10:754–762.

Tang W, Ehrlich I, Wolff SB, Michalski AM, Wolfl S, Hasan MT, Luthi A, Sprengel R. 2009. Faithful expression of multiple proteins via 2A-peptide self-processing: a versatile and reliable method for manipulating brain circuits. J Neurosci. 29:8621–8629.

Van Harreveld A. 1959. Compounds in brain extracts causing spreading depression of cerebral cortical activity and contraction of crustacean muscle. J Neurochem. 3:300–315.

Voipio J, Pasternack M, MacLeod K. 1994. Ion-sensitive microelectrodes. In: Ogden D, editors. The Plymouth Workshop Handbook, 2nd ed. Cambridge, UK: Company of Biologists. p 275–316.

Vyskocil F, Kritz N, Bures J. 1972. Potassium-selective microelectrodes used for measuring the extracellular brain potassium during spreading depression and anoxic depolarization in rats. Brain Res. 39:255–259.

Yaseen MA, Srinivasan VJ, Sakadzic S, Radhakrishnan H, Gorczynska I, Wu W, Fujimoto JG, Boas DA. 2011. Microvascular oxygen tension and flow measurements in rodent cerebral cortex during baseline conditions and functional activation. J Cereb Blood Flow Metab. 31:1051–1063.